Computers & Geosciences ∎ (∎∎∎∎) ∎∎∎–∎∎∎

Contents lists available at ScienceDirect

Computers & Geosciences

journal homepage: www.elsevier.com/locate/cageo

Hydrodynamic model calibration from pattern recognition of non-orthorectified terrestrial photographs

N. Pasquale [a,c], P. Perona [a,*], A. Wombacher [b], P. Burlando [c]

[a] Group AHEAD, Institute of Environmental Engineering, EPFL – ENAC, Lausanne, Switzerland
[b] Database Group, Faculty of Computer Science, University of Twente, Netherlands
[c] Institute of Environmental Engineering, ETH Zurich, Zurich, Switzerland

ARTICLE INFO

Article history:
Received 3 January 2013
Received in revised form
11 June 2013
Accepted 19 June 2013

Keywords:
Model calibration
Pattern recognition
Remote sensing
Non-orthorectified images
River restoration

ABSTRACT

This paper presents a remote sensing technique for calibrating hydrodynamics models, which is particularly useful when access to the riverbed for a direct measure of flow variables may be precluded. The proposed technique uses terrestrial photography and automatic pattern recognition analysis together with digital mapping and does not require image ortho-rectification. Compared to others invasive or remote sensing calibration, this method is relatively cheap and can be repeated over time, thus allowing calibration over multiple flow rates . We applied this technique to a sequence of high-resolution photographs of the restored reach of the river Thur, near Niederneunforn, Switzerland.

In order to calibrate the roughness coefficient, the actual exposed areas of the gravel bar are first computed using the pattern recognition algorithm, and then compared to the ones obtained from numerical hydrodynamic simulations over the entire range of observed flows. Analysis of the minimum error between the observed and the computed exposed areas show that the optimum roughness coefficient is discharge dependent; particularly it decreases as flow rate increases, as expected. The study is completed with an analysis of the root mean square error (RMSE) and mean absolute error (MEA), which allow finding the best fitting roughness coefficient that can be used over a wide range of flow rates, including large floods.

1. Introduction

The need for hydraulic simulations of river systems is important to explore the ecological role of low flows (e.g. Diez-Hernandez, 2008), to verify the inundation hazard in the floodplain at intermediate flows (e.g. Girard et al., 2010), as well as the hazard and the impact of flood waves (e.g. Junk et al., 1989, Di Baldassarre et al., 2009) and how to mitigate them (e.g. Bernardara et al., 2010).

The reliability of numerical hydraulic models depends on several factors and among them on how calibration is performed (e.g., Chow, 1973; Aronica, 1998; Horritt, 2004) ideally would require the use of flow-dependent roughness coefficients in order to adequately account for the role of submergence. However, the ability of finding a single roughness coefficient that works over multiple discharges is also important because it simplifies numerical operations. Recently, many authors have investigated the use of automatic techniques for calibrating hydrodynamic models. Such techniques are also often implemented for watershed models (e.g., Fabio et al., 2010).

Calibration methods can be classified in two main groups: traditional methods relying on field measurements (e.g., water depth, velocity and flooded area), and techniques based on remote sensing imagery. Both methods are based on an output error criterion, used to determine river bed roughness parameters.

Traditional methods (e.g., Beker and Yeh, 1972; Fread and Smith, 1978; Wasantha Lal, 1995; and Wohl, 1998), although very effective and still largely used to calibrate hydrodynamic models, are expensive, time consuming and often not practical. First, such measures represent only discrete information of the flow conditions for selected sections. Therefore, an accurate calibration requires as many observations as possible. In order to be representative of the flow conditions, the number of measures should increases in case of complex river sections such as braided rivers. Second, measuring flow depth or water surface elevation may be not practical, especially during high flow conditions, when the access to the river is difficult or even precluded for safety reasons.

More recently, non-invasive techniques based on remote sensing have tackled the problem by using aerial and satellite pictures. In recent studies, hydrodynamic models were calibrated by using either topographic information obtained from airborne laser altimetry (e.g., Cobby et al., 2001; Castellarin et al., 2009),

* Corresponding author. Tel.: +41 216933803
E-mail addresses: pasquale@ifu.baug.ethz.ch (N. Pasquale), paolo.perona@epfl.ch (P. Perona).

0098-3004/$ - see front matter © 2013 Elsevier Ltd. All rights reserved.
http://dx.doi.org/10.1016/j.cageo.2013.06.014

from satellite synthetic aperture radar (SAR) sensors (e.g., Horritt et al., 2007), or from inundation maps (e.g, Dung et al., 2011). However, inundation maps generated from a single observation often produce uncertain prediction (Aronica, 1998; Romanowicz and Beven, 1998, 2003; Aronica et al., 2002; Hall et al., 2005; Pappenberger et al., 2005). The use of aerial georeferenced images is another popular non-invasive technique, which usually relies on just one shot for economic reasons. Hence, no information about varying flow condition is available. Forzieri et al. (2010) calibrated a 1-D numerical hydraulic model on the basis of Quickbird images of a river reach riparian area and LIDAR data, showing the effect of different type of vegetation classes and patterns on the hydraulic roughness parameter. Other works combined velocity measurement using LS-PIV (e.g., Muste et al., 2008; Hauet et al., 2008, 2009; Jodeau et al., 2008; LeCoz et al., 2010), and ortho-rectification of ground-based images (often with very flat shooting angle) using photogrammetric equations in order to link reference points of known coordinates in both image and real world systems.

In order to have a reliable control of the calibration process, field measurements, at different spatial and time scales, are always recommended. Field work and remote sensing techniques are two methodologies that efficiently complete each other in field scale numerical hydrodynamic modeling studies.

This study addresses a terrestrial photography technique, which uses low cost digital images of the investigated river reach and obtains from them flow rate versus inundated area relationship. By comparing the simulation of the inundated area to that visible in the pictures taken at a known flow rate, the calibration of the riverbed roughness, expressed as flow-dependent Manning's roughness coefficient (e.g., Aronica, 1998) is performed. Moreover, an error statistical analysis allows highlighting a single roughness coefficient that can be used over a wide range of flow rates. This method is not expensive since the photographs used for the calibration are taken from a high resolution, but common digital camera. Moreover, the fact that no image orthorectification is needed, offers a new perspective of calibration and validation of 2-D numerical hydraulic models, which can be applied to several flow conditions, including flood events.

2. Material and methods

2.1. Study site and monitoring devices

The Thur is a perennial river in the north-eastern part of Switzerland (Fig. 1a) characterized by a nivo-pluvial hydrological regime. The catchment area (Fig. 1b) is about 1750 km^2 and the river has a length of about 127 km. It is the longest river in Switzerland that flows continuously without any regulation by artificial reservoirs or natural lakes (Pasquale et al., 2011).

The hydrologic regime of the Thur shows the presence of rapid floods particularly during springtime and autumn, when flood pulses are generated as a combination of snow melt and intense precipitation. Discharge may increase dramatically within a few hours and trig both bed load and suspended sediment transport. The mean annual discharge is 47 m^3/s. Observed low flows can be as low as 2.2 m^3/s. Flows with return period of 2, 10 and 100 years, at the gauging station located 15 km downstream the restored reach, are estimated respectively 570 m^3/s, 820 m^3/s and 1070 m^3/s[1] .

The Thur River was channelized in the past century to improve flood protection, to increase agriculture areas and to reduce spreading of disease. Since the '90 s several corrections equally promoted river restoration and flood protection measures. In 2002, a 2 km long reach near Niederneunforn was modified by removing lateral bank protections (Fig. 1c). As a consequence, an active alternate bar system developed as the river locally widened (Pasquale, 2012). The mean river bed slope in the non-restored reach is in the order of 0.16%. Fig. 1d shows an aerial view of the restored reach in 2009, and two representative cross section of the restored reach (Fig. 1e, f) to compare with a regular section of the straight channel upstream (Fig. 1g). River bathymetry is manually measured along river cross sections located at maximum 25 m distance to each other and one point each 50 cm approximately. High resolution Digital Terrain Model (DTM) are also produced from LIDAR flights once a year under autumn low flow conditions. The original planimetric accuracy of the DTM is ± 5 cm while the vertical precision is in the order of ± 10 cm.

In order to produce a continuous time series of terrestrial photographs of the bar shown in Fig. 1d, we installed one digital camera (NIKON D300) within a box on the top of a monitoring tower located 16 m above the levee level on the left side of the river (Fig. 1d, see also Pasquale et al., 2011). The digital camera is connected to a remote computer, from which it is possible to change the shooting frequency in order to better capture the evolution of floods events . Three representative photographs are shown in Fig. 2a, b, c. Such images show that only few flexible vegetation spots colonize the emerging bedforms, thus not contributing too much to the equivalent mean riverbed roughness.

Two gauging stations located few kilometers upstream and downstream of the restored reach record hourly discharge. Discharge data as well as rating curves, topographic information of the measuring site as well as hydrological data are also available via the Federal Office for the Environment (FOEN) webpage (http://www.hydrodaten.admin.ch/en/2044.html).

In order to characterize the grain size distribution of river bed of the restored reach, analyses of the grain size distribution were carried out in 2009. Results, also published by Pasquale et al. (2011) show a strong vertical sorting with higher percent of coarse sediment on the bedform surface (Fig. 3). Moreover, also in accordance with other experimental observations (Lisle et al., 1991; Diplas and Parker, 1992; Lisle and Madej, 1992 and Ashworth et al., 1992), the island is characterized by a longitudinal sorting. From coarse particle deposition upstream (d_{50}=1.0–5.0 cm) we move to fine sand deposition downstream (d_{50}=0.2 cm), where stratification also is not anymore evident (Pasquale et al., 2011).

2.2. Numerical hydrodynamic model

We used the freely available 2-D numerical hydrodynamic model BASEMENT (Faeh et al, 2010) developed at ETH Zurich (http://www.basement.ethz.ch/) which numerically integrates the shallow water equations using the finite volume method, and has extensively been tested for scientific and professional purposes (Beffa and Cornell, 2001a, b; Schäppi et al., 2010; Schneider et al., 2011; Pasquale et al., 2011, 2012; Pasquale, 2012).

Simulations were run on an unstructured irregular mesh built on the yearly recorded DTM, and corrected to include actual river cross sections as described by Schäppi et al. (2010). Recorded hourly discharge data were used as input together with suitable boundary and initial conditions (Pasquale et al., 2011; Pasquale, 2012).

Flow dynamics is modeled using the shallow water equations approximation:

$$\frac{\partial h}{\partial t}+\frac{\partial(\overline{u}h)}{\partial x}+\frac{\partial(\overline{v}h)}{\partial y}=0 \quad (1a)$$

[1] Federal Office for the Environment, http://www.hydrodaten.admin.ch/en/2044.html.

Please cite this article as: Pasquale, N., et al., Hydrodynamic model calibration from pattern recognition of non-orthorectified terrestrial photographs. Computers & Geosciences (2013), http://dx.doi.org/10.1016/j.cageo.2013.06.014

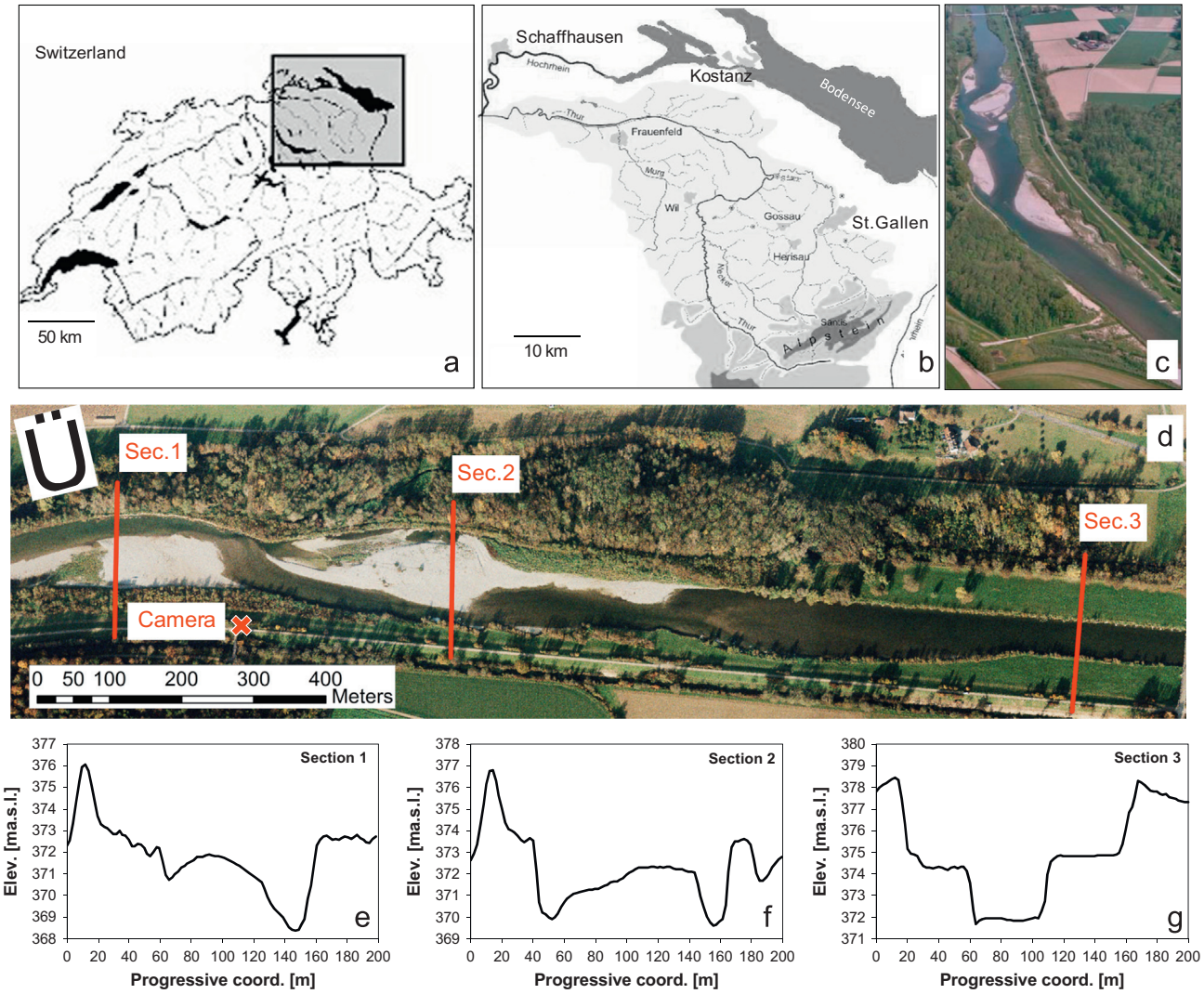

Fig. 1. Thur river watershed and location in NE Switzerland (a, b). Aerial view of the restored corridor in 2005 (c). Aerial view of the study site in 2009 within the restored reach of the Thur River (d). Frame e, f, g show, respectively, two explicative cross section in the restored corridor and one section, more regular, in the straight reach upstream.

Fig. 2. Three representative pictures taken from the digital camera at 20 m^3/s (b), 100 m^3/s (c), and 250 m^3/s (d), in 2009, show how the access to the river becomes impossible at high flow rates.

$$\frac{\partial \bar{u}}{\partial t}+\bar{u}\frac{\partial \bar{u}}{\partial x}+\bar{v}\frac{\partial \bar{u}}{\partial y}+g\frac{\partial h}{\partial x}=-g\frac{\partial z_b}{\partial x}-\frac{1}{\rho h}\tau_{bx}+\frac{1}{\rho h}\frac{\partial[h(\bar{\tau}_{xx}+D_{xx})]}{\partial x}+\frac{1}{\rho h}\frac{\partial[h(\bar{\tau}_{xy}+D_{xy})]}{\partial y} \quad (1b)$$

$$\frac{\partial \bar{v}}{\partial t}+\bar{u}\frac{\partial \bar{v}}{\partial x}+\bar{v}\frac{\partial \bar{v}}{\partial y}+g\frac{\partial h}{\partial y}=-g\frac{\partial z_b}{\partial y}-\frac{1}{\rho h}\tau_{by}+\frac{1}{\rho h}\frac{\partial[h(\bar{\tau}_{yx}+D_{yx})]}{\partial x}+\frac{1}{\rho h}\frac{\partial[h(\bar{\tau}_{yy}+D_{yy})]}{\partial y} \quad (1c)$$

where h is the water depth (m), g the gravity acceleration (m/s^2), ρ the water density (kg/m^3), $\bar{u}$ and $\bar{v}$ the depth averaged velocities in x- and y-directions (m/s), Z_b the bottom elevation (m), τ_{bx} and τ_{by} the bed shear stresses in x- and y-direction (N/m^2), $\bar{\tau}_{ij}$ the depth averaged turbulent and viscous stresses (N/m^2), $D_{i,j}$ the momentum dispersion terms (at the moment not explicitly modeled in Basement). Turbulent and viscous shear stresses are quantified according to the Boussinesq eddy viscosity hypothesis (Boussinesq, 1877; Schmitt, 2007) and the quadratic friction law to relate bed shear

Please cite this article as: Pasquale, N., et al., Hydrodynamic model calibration from pattern recognition of non-orthorectified terrestrial photographs. Computers & Geosciences (2013), http://dx.doi.org/10.1016/j.cageo.2013.06.014

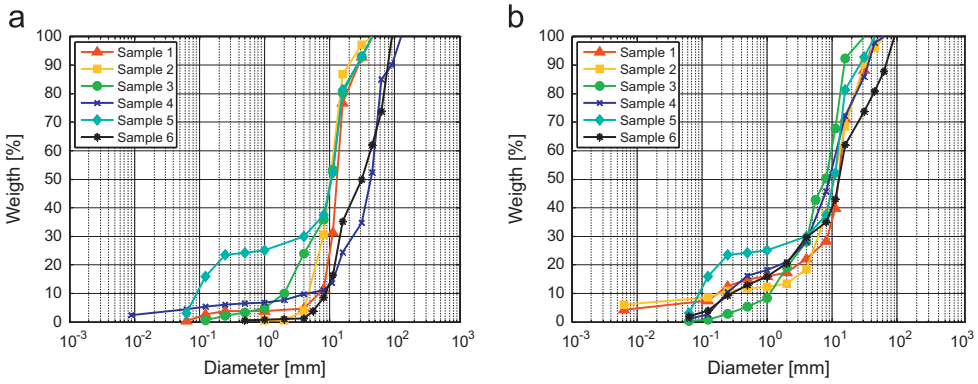

Fig. 3. Grain Size Distributions for the six different locations on the main island of the restored reach. Samples were taken on the surface (a) and at 40 cm depth (b). d_{50} and d_{90} are generally higher on surface layers (b) than at 40 cm (b). Surface samples (a) show also a higher spatial sediment sorting, from coarser material upstream (sample 6) to finer material downstream (sample 5). Sediments at 40 cm depth are more spatially similar and d_{50} is practically equal for all samples (b). Comparing (a) and (b) it is evident the vertical sorting typical of river bed forms.

stresses and depth averaged velocities:

$$\tau_{Bx} = \rho \frac{|U|u}{c_f^2}, \tag{2a}$$

$$\tau_{By} = \rho \frac{|U|v}{c_f^2} \tag{2b}$$

in which $|U|$ is the magnitude of the velocity vector and c_f the non dimensional Chézy friction coefficient, related to the Manning's roughness coefficient n by $c_f^2 = R^{1/3}/gn^2$.

All simulations were run by starting from an initial condition of dry bed cells, and by waiting until steady the state in the whole domain was reached, i.e., when the outboundary flow became constant and equal to the inflow boundary condition.

The upstream boundary condition was set by imposing the flow rate and the corresponding water depth, as observed in a almost regular cross section upstream the Altikon bridge. As downstream boundary condition a weir was set as this corresponds to a physical condition actually present in the riverbed (weir height = 50 cm). The presence of the weir was however not influent on the hydrodynamics of the restored reach upstream under all the investigated flow rates.

3. Pattern recognition and calibration technique

The calibration technique described in this work consists of three steps: (i) pattern recognition, (ii) digital mapping and (iii) model fitting. To illustrate the procedure, we refer here to the sequences of terrestrial pictures shown in Fig. 2.

STEP 1 The first step requires the recognition and extraction of river bed forms such as bars and islands from selected terrestrial photographs under different flow conditions. We developed an automatic recognition procedure to classify the pixels with the highest probability of being non-water, which represents the island surface and the surrounding shore areas. While the first version of the automatic classifier presented by Pasquale et al. (2011) required a large amount of training classified data, the approach presented here is improved and does not require this anymore. The classification approach is based on six features that we use in order to recognize either natural or geometrical elements in the photograph (e.g., bare soil, water, shorelines, etc…). Hence, this method performs similarly to the approaches used by autonomous off-road navigation (Rankin et al., 2004) and on water level detection (Iwahashi and Udomsiri, 2007). The first feature classifies the bare soil on the island and it is a combination of image saturation and of the HSV (Hue Saturation Value) representation of the image. Features two, three and four are used to classify vegetation and the shoreline of the island. In particular, the second feature is based on the amount of edges detected in the image. The third feature is based on the difference between hue and the HSV representation of the image, while the forth feature is based in the difference between green and blue channel of the RGB representation of the image. The last two features are error prone since they also classify reflections of vegetation in the water as non-water under certain conditions. Fig. 4 shows an example of the output results. At the present stage, the method allows recognizing and classifying with satisfactory precision the non-water pixels, represented by the red masked areas.

STEP 2 The second step is the digital mapping and consists of building a metric to compute the actual area of the island as seen through a perspective view point, that is obtaining the actual area from pixels of the 2D non-orthorectified digital image. This task was achieved by positioning two rectangular tarps of known and different areas (blue, 5.1 m^2 and green, 10.9 m^2) at 18 different locations on the reference island (Fig. 5a). We chose the locations in order to almost uniformly cover the entire island and for each of them, a photograph was taken in August 2009 under homogenous conditions of light and flow (Fig. 5b). We developed a Matlab® script to compute the number of pixels (RGB channels) that each tarp occupies in each photograph. Thus, by knowing the actual area of the tarps, a Pixel-to-Area ratio (PA, [m^2/pixel]) could be calculated for each tarp location and each picture. The final pixel-to-area ratio at each location is the average of the ratios of the blue and green tarps at the same location. The average values of the two tarps at each of the 18 locations are associated to the averaged center of area of the tarps (Table 1). The pixel-to-area conversion ratio for every pixel of the island is then obtained by fitting a second order polynomial to the values computed for each (ξ, η) coordinate of the tarp locations:

$$PA(\xi,\eta) = a\xi^2 + b\eta^2 + c\xi\eta + d\xi + e\eta + f, \tag{3}$$

where ξ, η are the coordinate of each pixel of the photograph and a, b, c, d, e and f are fitting parameters given by the regression analysis ($a = -7.46 \times 10^{-09}$, $b = 1.27 \times 10^{-07}$, $c = -7.48 \times 10^{-08}$, $d = 1.59 \times 10^{-04}$, $e = -4.97 \times 10^{-04}$,

Please cite this article as: Pasquale, N., et al., Hydrodynamic model calibration from pattern recognition of non-orthorectified terrestrial photographs. Computers & Geosciences (2013), http://dx.doi.org/10.1016/j.cageo.2013.06.014

Fig. 4. The automatic algorithm for pattern recognition allows delimitation of water and non-water classes from digital photographs. The reddish mask over the pictures represents the pixels classified as non-water.

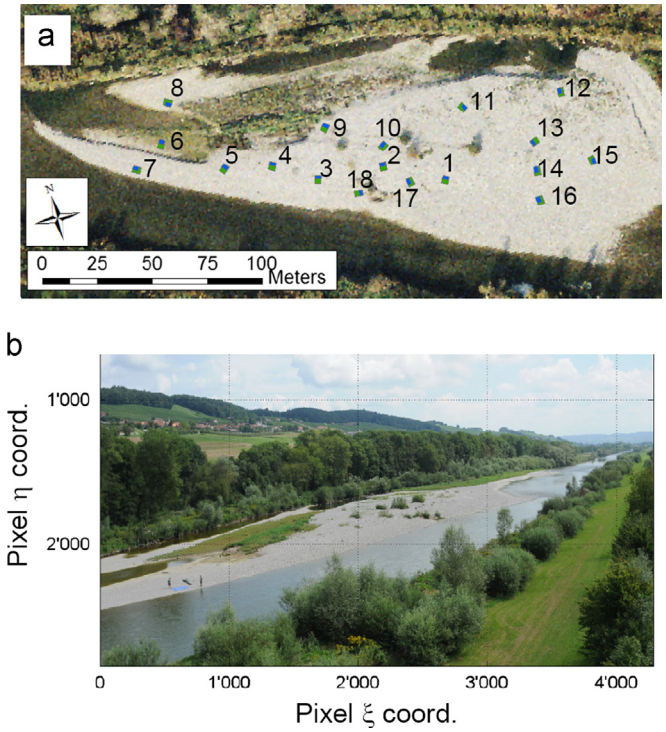

Fig. 5. Aerial photo of the research island in 2009 with the green and blue tarps (a). Coordinate are in meters (E, N). Example of photograph used for the calibration (b). The discharge represented in the picture is 20 m^3/s and the coordinate are in pixel number.

$f = 4.9 \times 10^{-01}$). The value of the corresponding coefficient of determination (R^2_{adj}) is equal to 0.93. At this point, for a given picture we know the 2D area of the island (delimited by a shoreline) through the automatic pattern recognition. A last step is necessary in order to crop the island surface from the original picture thus defining the domain of validity of the (3). This is done manually. The cropped area (Fig. 6a) is the domain ω of the function PA by means of which we convert each pixel within ω into an actual area. The integral computed over the domain ω delimited by the shoreline of the function PA(ξ, η) gives the total area of the island A:

$$A = \iint_{\omega} PA(\xi,\eta)d\xi\, d\eta. \quad (4)$$

An example of the conversion ratio (in m^2) for each pixel of the research island is shown in Fig. 6b, whereas the comparison between the observed pixel-to-area conversion and the estimated one is shown in Fig. 6c.

STEP 3 The third step consists of comparing the area of the island obtained in the steps 1 and 2 for different flow rates, assuming steady state conditions, with that obtained by the 2D hydrodynamic simulation, for different values of the Manning's coefficient n. The calibration is done by choosing the value of n that best matches the simulated island area with the one obtained through photographs. We used a homogeneous roughness coefficient, which was allowed to change in the range $n = 0.017 \div 0.028$ $m^{-1/3}s$, in order to remain within reasonable values of the physical roughness. Simulations were run for six different discharges (ranging in the interval $Q = 20 \div 250$ m^3/s) corresponding to two limits where the errors resulting in the stream size and the island size start influencing the results. The first one is essentially due to the accuracy of the adopted DEM, whereas the second one is ascribable to the extremely small size of the sediment that remains exposed compared to the camera resolution (12 MP).

The output in terms of water surface elevation was imported in a GIS environment to compute the area of the research island (simulated by the model) and to compare it with the actual area computed from digital image (steps 1 and 2) at the same flow rate. The results and the percentage errors for varying Manning's coefficients n are shown in Table 1, and will be further discussed in Section 4.

4. Results and discussion

By comparing the percentage error between simulated and observed areas for different Manning's n, we found the roughness coefficient that minimizes such error at a given discharge (Table 1). At high flow rate the progressive decrease of the exposed area of the gravel bar makes the conversion pixel-to-area gradually less precise. Similarly for low flows the amount of the island area not visible by the camera leads to a systematic overestimation of the observed area versus the simulated one. Fig. 7a shows an interesting result clearly reflecting the role of the relative submergence, i.e. the ratio between the equivalent sediment diameter and the average flow depth. As expected, riverbed roughness decreases as the discharge increases. At low flow rates indeed (Fig. 7a, $Q < 60$ m^3/s), grain size is the main factor influencing the roughness coefficient (e.g., Julien, 1995; Bathurst, 2002). This is due to shallow submergence, when the relative roughness ε (the ratio between mean sediment diameter d and water depth h) is between 0.01 and 0.1. As discharge increases, h increases too and therefore the relative roughness decreases. At high flow rates ($Q > 200$ m^3/s) when most of bed forms are submerged the grain size has, generally, less effect on the river roughness which is rather influenced at large scale by river bed forms (Julien, 1995).

Please cite this article as: Pasquale, N., et al., Hydrodynamic model calibration from pattern recognition of non-orthorectified terrestrial photographs. Computers & Geosciences (2013), http://dx.doi.org/10.1016/j.cageo.2013.06.014

Table 1
Manning's n of the roughness coefficients used for calibration. The table shows also the discharges range of value simulated and the corresponding area of the island produced and the related error.

	Q=20 m³/s A_{photo}=13880 m²		Q=60 m³/s A_{photo}=9539 m²		Q=100 m³/s A_{photo}=8328 m²		Q=140 m³/s A_{photo}=6394 m²		Q=200 m³/s A_{photo}=3666 m²		Q=250 m³/s A_{photo}=1780 m²	
n [$m^{-1/3}s$]	A_{sim} [m^2]	Error [%]	A_{sim} [m^2]	Error [%]	A_{sim} [m^2]	Error [%]	A_{sim} [m^2]	Error [%]	A_{sim} [m^2]	Error [%]	A_{sim} [m^2]	Error [%]
0.017	15560	10.8	10868	12.2	8596	3.1	6968	8.2	3712	1.2	1500	-18.7
0.018	15480	10.3	10700	10.9	8544	2.5	6712	4.7	3604	−1.7	1376	−29.4
0.019	15424	10.0	10460	8.8	8490	1.9	6580	2.8	3412	−7.4	1244	−43.1
0.020	15364	9.7	10404	8.3	8440	1.3	6372	−0.3	3216	−14.0	1144	−55.6
0.021	15304	9.3	10356	7.9	8316	−0.1	6124	−4.4	3048	−20.3	1028	−73.2
0.022	15104	8.1	10092	5.5	8024	−3.8	5976	−7.0	2928	−25.2	848	−109.9
0.023	15012	7.5	10056	5.1	7888	−5.6	5832	−9.6	2860	−28.2	680	−161.8
0.024	14828	6.4	9984	4.5	7464	−11.6	5752	−11.2	2548	−43.9	488	−264.8
0.025	14824	6.4	9752	2.2	7272	−14.5	5652	−13.1	2324	−57.7	436	−308.3
0.026	14804	6.2	9620	0.8	7120	−17.0	5392	−18.6	2080	−76.3	372	−378.5
0.027	14688	5.5	9564	0.3	7024	−18.6	5248	−21.8	1876	−95.4	308	−477.9
0.028	14624	5.1	9500	−0.4	6828	−22.0	4912	−30.2	1728	−112.2	288	−518.1

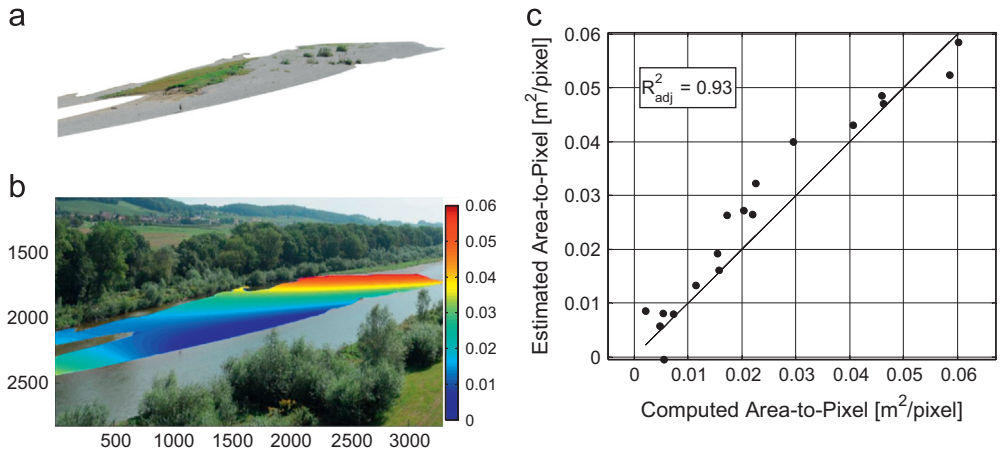

Fig. 6. On the basis of the results shown in Fig. 2 the area of the island is then extracted manually (a) and used as a boundary ω for the second order polynomial interpolation function (Eq.(3)). Eq.(3) computed over the boundary ω gives the pixel-to-area (PA) conversion for each pixel of the surface (b). The coefficient of determination, computed for the observed value of the pixel-to-area conversion and the estimated ones (c).

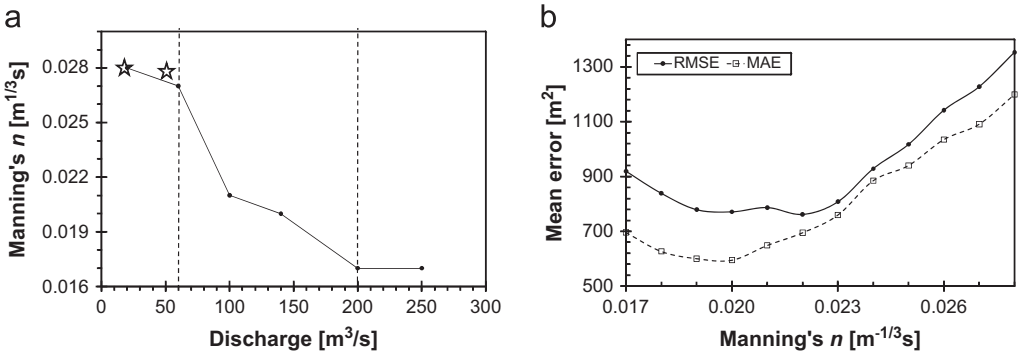

Fig. 7. Plot (a) represents the best roughness values for each discharge. The optimum value changes according to the flow rate. Stars represent the calibrated values obtained from dGPS survey of the island shoreline at 15 m^3/s and 50 m^3/s. Chart of the mean errors computed for all flow rates using Eqs. (5) and (6) (b).

From Fig. 7a, in correspondence of abrupt gradient changes of the plot, three different ranges of n can be identified: for $Q < 60\ m^3/s$, the average n is equal to $0.0275\ m^{-1/3}s$, for $60 < Q < 180\ m^3/s$, the average n is $0.022\ m^{-1/3}s$ for $Q > 180\ m^3/s$, $n = 0.017\ m^{-1/3}s$. The set of pictures that we used for calibration allowed considering only discharges lower than $300\ m^3/s$. This is indeed the critical discharge for which all river bed forms are submerged and therefore, not visible in the picture anymore. Fig. 7a suggests that, for discharges higher than $250\ m^3/s$, the relation between roughness coefficient and discharge is likely to become

Please cite this article as: Pasquale, N., et al., Hydrodynamic model calibration from pattern recognition of non-orthorectified terrestrial photographs. Computers & Geosciences (2013), http://dx.doi.org/10.1016/j.cageo.2013.06.014

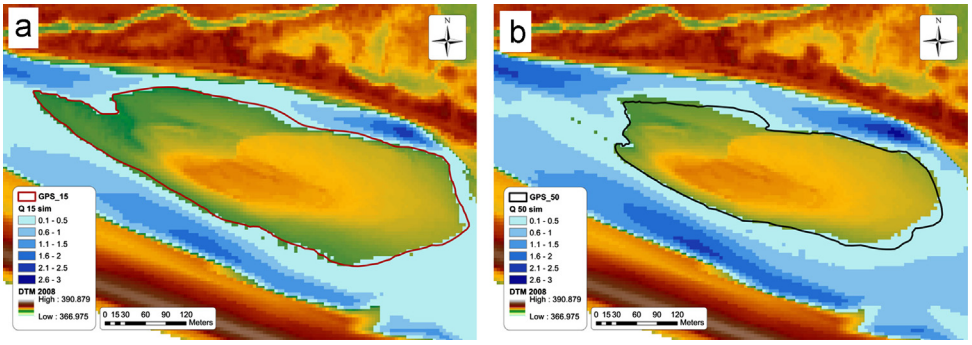

Fig. 8. Simulations run for topography 2008 at 15 m^3/s (a) and 50 m^3/s (b) show the comparison between the observed island shoreline (measured by a differential GPS) and the simulated one.

asymptotic. At present we cannot advance any conclusion in this direction, but we would rather expect that the effects of submerged bedforms and bank vegetation start playing a role and determine a successive increase of the equivalent roughness.

In order to identify an equivalent roughness value to be used for all investigated flow rates, we adopted two statistical measures, the root mean square error (RMSE) and the mean absolute error (MAE), as suggested for instance by Papanicolau et al. (2011). There are respectively defined as:

$$RMSE = \sqrt{\frac{1}{N}\sum_{j}^{N}(O_j - S_j)^2} \tag{5}$$

$$MAE = \frac{1}{N}\sum_{j}^{N}\left|O_j - S_j\right| \tag{6}$$

where N is the number of field measurements, O_j are the observed values and S_j are the simulated areas. The lower these errors are, the better simulated values fit observed ones. The plot of RMSE and MAE vs. n (Fig. 7b) shows that the best n value is 0.020 $m^{-1/3}s$ according to MAE, and it is 0.022 $m^{-1/3}s$ according to RMSE.

We use the equation $n = 0.0417 d_{50}^{1/6}$ (Chow, 1973) to compute the theoretical d_{50} corresponding to the roughness coefficient determined from the calibration. In the range of $0.017 < n < 0.028$ $m^{-1/3}s$ (Fig. 7), Chow's equation leads to $0.5 < d_{50} < 9.2$ cm, particularly to $d_{50} = 2.2$ cm for $n = 0.022$ $m^{-1/3}s$. This value is in substantial agreement with the grain size curve (Fig. 3) showing that the median grain size d_{50} ranges in the interval $1.0 \div 4.5$ cm. Also, Julien (2002) suggests for river with gravel bars a value of the Manning's coefficient ranging in the interval $0.012 < n < 0.030$ $m^{-1/3}s$. In contrast, Chow (1973) reports that for clean, straight, full stage, no rifts or deep pools natural streams, the manning's coefficient ranges from 0.025 $m^{-1/3}s$ to 0.033 $m^{-1/3}s$, with average of 0.030 $m^{-1/3}s$. Eventually, our technique can be considered as a validation tool to post-verify whether the adopted roughness on the base of empirical relationships (e.g., Chow equations) produces results that are compatible with the real stream behavior.

As a validation test, we verified the model performances by simulating the discharges of 15 m^3/s and 50 m^3/s on a mesh built for the previous year topography (i.e., on the DTM made in 2008) and by using the roughness coefficients suggested by Table 1 for those river discharges. For this year, precise measurements of the island shoreline for those flow rates were available from manually performed differential GPS surveys. Results are shown in Fig. 8a, b, which in both cases show a very good overlap of the measured and the computed shorelines. Notably, the two star points in Fig. 7b show that the roughness coefficient ($n = 0.028$ $m^{-1/3}s$), obtained by calibrating the model against the GPS surveyed island shoreline for the two available flow rates of 15 and 50 m^3/s, is in accordance with the ones obtained with the proposed technique.

Considering the uncertainties in calculating Manning's roughness from empirical relationships depending only on roughness height (the aforementioned values range from 0.017 to 0.028 $m^{-1/3}s$), the proposed technique can be considered a valuable alternative to standard methodologies or LS-VIP methods. Indeed, due to the irregular topography of the restored reach and its large scale, calibration based on both traditional techniques and LS-VIP would need several scaled-rods positioned at different locations. Installing them on the island is often not allowed, with the further risk that poles may easily bend, break or be removed during floods. Moreover, the distance between the camera and the monitored river reach (in our case $150 \div 300$ m) may result in a resolution not enough detailed to allow reading scale bars on the rods and installation of cameras to closer distances would not be allowed by river management authorities.

5. Conclusions

We presented a methodology to calibrate 2-D numerical hydrodynamic models from non-orthorectified terrestrial photographs, which can be considered a non-invasive, economically cheap alternative to both traditional and recent airborne-laser-based techniques. Assuming that the average grain size of the alluvial sediment is not time dependent, and that only the grain size distribution of bed load transport is flow rate dependent (Parker et al, 2008; Viparelli et al, 2011), the digital mapping function in principle can be implemented only once, i.e. at very low flow conditions. This metric is then used to convert 2D photographs into actual river bed forms area that is exposed under certain flow conditions. This methodology allows then extracting the optimal equivalent roughness coefficient for each flow rate, or even the best one that can be used over a desired range of discharges. The possibility of using a unique roughness coefficient is particularly useful to simulate discharges for which field measurements may be precluded, due to security reasons.

The spatial scale over which the method is applicable is related to the resolution of the camera. Also, some hints should be considered for further improvements of this technique: the number of tarp locations should be as big as possible, especially far from the camera where the mapping function converting pixels to actual area gives high errors. In alternative, the analyzed area should be contained within a small distance from the camera to avoid low visibility of far tarps.

Please cite this article as: Pasquale, N., et al., Hydrodynamic model calibration from pattern recognition of non-orthorectified terrestrial photographs. Computers & Geosciences (2013), http://dx.doi.org/10.1016/j.cageo.2013.06.014

Acknowledgments

This study was financed by the CCES of the ETH domain in the framework of the RECORD project (http://www.cces.ethz.ch/projects/nature/Record). Thanks also to Umberto Villero for his help with the simulations in BASEMENT. Paolo Perona thanks the Swiss National Science Foundation for financial support (Grant No. PP00P2–128545/1).

References

Aronica, G., 1998. Uncertainty and equifinality in calibrating distributed roughness coefficients in a flood propagation model with limited data. Advances in Water Resources 22 (4), 349–365.

Aronica, G., Bates, P.D., Horritt, M.S., 2002. Assessing the uncertainty in distributed model predictions using observed binary pattern information within GLUE. Hydrological Processes 16 (10), 2001–2016.

Ashworth, P.J., Ferguson, R.I., Powell, M.D., 1992. Bedload transport and sorting in braided channels. In: Billi, P., Hey, R., Thorne, C., Tacconi, P. (Eds.), Dynamics of Gravel-bed Rivers. John Wiley & Sons LTD., Chichester, pp. 497–515.

Bathurst, J.C., 2002. A-a-site variation and minimum flow resistance for mountain rivers. Journal of Hydrology 269, 11–26.

Beffa, C., Cornell, R.J., 2001a. Two-dimensional flood plain flow. I Model description. Journal of Hydraulic Engineering 6 (5), 397–405.

Beffa, C., Cornell, R.J., 2001b. Two-dimensional flood plain flow. II. Model validation. Journal of Hydrological Engineering 6 (5), 405–415.

Beker, L., Yeh, W.W.-G., 1972. Identification of parameters in unsteady open channel flows. Water Resources Research 8 (4), 956–965.

Bernardara, P., de Rocquigny, E., Goutal, N., Arnaud, A., Passoni, G., 2010. Uncertainty analysis in flood hazard assessment: hydrological and hydraulic calibration. Canadian Journal of Civil Engineering 37, 968–979.

Boussinesq, J., 1877. Essai sur la théorie des eaux courantes. Mémoires présentés par divers savants à l'Académie des Sciences XXIII 1, 1–680.

Castellarin, A., Di Baldassarre, G., Bates, P.D., Brath, A., 2009. Optimal cross-sectional spacing in preissmann scheme 1D hydrodynamic models. Journal of Hydraulic Engineering 135 (2), 96–105.

Chow, V.T., 1973. Open-channel Hydraulics. McGraw-Hill Book, New York p. 680.

Cobby, D., Manson, D.C., Davenport, I.J., 2001. Image processing of airborne scanning laser altimetry data for improved river flood modelling. ISPRS Journal of Photogrammetry and Remote Sensing 56 (2), 121–138.

Di Baldassarre, G., Schumann, G., Bates, P., 2009. A technique for the calibration of hydraulic models using uncertain satellite observations of flood extent. Journal of Hydrology 367 (3–4), 276–282.

Diez-Hernandez, J.M., 2008. Hydrodynamic ecohydraulic habitat assessment aimed at conserving and restoring fluvial hydrosystems. Ingeniería e Investigación 28 (2), 97–107.

Diplas, P., Parker, G., 1992. Deposition and removal of fines in gravel-bed streams. In: Billi, P., Hey, R.D., Thorne, C.R., Tacconi, P. (Eds.), Dynamic of Gravel-bed Rivers. John Wiley and Sons LTD, Chichester, pp. 313–329.

Dung, N.V., Merz, B., Bárdossy, A., Thang, T.D., Apel, H., 2011. Multi-objective automatic calibration of hydrodynamic models utilizing inundation maps and gauge data. Hydrology and Earth System Sciences 15, 1339–1354.

Fabio, P., Aronica, G.T., Apel, H., 2010. Towards automatic calibration of 2D flood propagation models. Hydrology and Earth System Sciences 14, 911–924.

Faeh R., Mueller R., Rousselot P., Veprekand R., Vetsch D, Volz C. Basement-basic simulation environment for computation of environmental flow and natural hazard simulation. Software manual. ETH Zurich, VAW, 2010. Available from: www.basement.ethz.ch.

Fread, D.L., Smith, G.F., 1978. Calibration techniques for 1-D unsteady flow models. Journal of the Hydraulics Division, ASCE 104 (7), 1027–1043.

Forzieri, G., Moser, G., Vivoni, E.R., Castelli, F., Canovaro, F., 2010. Riparian vegetation mapping for hydraulic roughness estimation using very high resolution remote sensing data fusion. Journal of Hydraulic Engineering 136 (11), 855–867.

Girard, P., Fantin-Cruz, I., Loverde de Oliveira, S.M., Hamilton, S.K., 2010. Small-scale spatial variation of inundation dynamics in a floodplain of the Pantanal (Brazil). Hydrobiologia 638, 223–233.

Hall, J.,W., Tarantola, S., Bates, P.,D., Horritt, M.,S., 2005. Distributed sensitivity analysis of flood inundation model calibration. Journal Hydraulic Engineering 131 (2), 117–126.

Hauet, A., Kruger, A., Krajewski, W.F., Bradley, A., Muste, M., Creutin, J.D., Wilson, M., 2008. Experimental system for real-time discharge estimation using an image-based method. Journal of Hydrologic Engineering 2, 105–110.

Hauet, A., Muste, M., Ho, H-C., 2009. Digital mapping of riverine waterway hydrodynamic and geomorphic features. Earth Surface Processes and Landforms 34, 242–252.

Horritt, M.A., 2004. Development and testing of a simple 2D finite volume model of a sub-critical shallow water flow. Journal for Numerical Methods in Fluids 44, 1231–1255.

Horritt, M.S., Di Baldassarre, G., Bates, P., Brath, A., D., 2007. Comparing the performance of a 2-D finite element and a 2-D finite volume model of floodplain inundation using airborne SAR imagery. Hydrological Processes 21, 2745–2759.

Iwahashi, M., Udomsiri, S., 2007. Water Level Detection from Video with Fir Filtering. ICCCN, IEEE, 826–831.

Jodeau, M., Hauet, A., Paquier, A., LeCroz, J., Dramais, G., 2008. Application and evaluation of LS-VIP technique for the monitoring of river surface velocities in high flow conditions. Flow Measurements and Instrumentation 19, 117–127.

Julien, P.Y., 1995. Erosion and Sedimentation, 1st Ed. Cambridge University Press, New York, USA p. 280.

Julien, P.Y., 2002. River Mechanics, 1st Ed. Cambridge University Press, Cambridge, United Kingdom p. 434.

Junk, W.J., Bayley, P.B., Sparks, R.E., 1989. The flood pulse concept in river-floodplain systems. Canadian Special Publication of Fisheries and Aquatic Sciences 106, 110–127.

LeCoz, J., Hauet, A., Pierrefeu, G., Dramais, G., Camenen, B., 2010. Performance of image-based velocimetry (LSPIV) applied to flash-flood discharge measurements in Mediterranean rivers. Journal of Hydrology 394, 42–52.

Lisle, T.E., Ikeda, H., Iseya, F., 1991. Formation of stationary alternate bars in a steep channel with mixed-size sediment—a flume experiment. Earth Surface Processes Landforms 16 (5), 463–469.

Lisle, T.E., Madej, A.M., 1992. Spatial variation in armoring in a channel with high sediment supply. In: Billi, P, Hey, R.D., Thorne, C.R., Tacconi, P. (Eds.), Dynamics of Gravel-bed Rivers. John Wiley and Sons LTD, Chichester, pp. 277–293.

Muste, M., Fujita, I., Hauet, A., 2008. Large-scale particle velocimetry for measurements in riverrine environments. Water Resources Research 44 (WOOD19), 1–19.

Papanicolau, A.N., Elhakeem, M., Wardman, B., 2011. Calibration and verification of a 2D hydrodynamic model for simulating flow around emergent bendway weir structures. Journal of Hydraulic Engineering 137 (1), 75–89.

Pappenberger, F., Beven, K., Horritt, M., Blazkova, S., 2005. Uncertainty in the calibration of effective roughness parameters in HEC-RAS using inundation and downstream level observations. Journal of Hydrology 302 (1–4), 46–69.

Parker, G., Hassan, M., Wilcock, P.R., 2008. Adjustment of the bed surface size distribution of gravel-bed rivers in response to cycled hydrographs. In: Habersack, H., Piegay, H., Rinaldi, M. (Eds.), Gravel-Bed Rivers VI: From Processes Understanding River Restoration. Elsevier, New York, pp. 241–285.

Pasquale, N., Perona, P., Schneider, P., Shrestha, J., Wombacher, A., Burlando, P., 2011. Modern comprehensive approach to monitor the morphodynamic evolution of restored river corridors. Hydrology and Earth System Sciences 15, 1197–1212.

Pasquale, N., Perona, P., Francis, R., Burlando, P., 2012. Effects of stream flow variability on the vertical root density distribution of willow cutting experiments. Ecological Engineering 40, 167–172.

Pasquale, N., 2012. Quantification of Vegetation Root Induced Cohesion in Non-cohesive River Beds by Experiments, Monitoring and Modeling. Ph.D. Thesis, ETH Zurich, Zurich, Switzerland.

Rankin, A.L., Matthies, L.H., Huertas, A., 2004. Daytime water detection by fusing multiple cues for autonomous Off-Road Navigation. DTIC and NTIS, Jet Propulsion LAB Pasadena, CA.

Romanowicz, R., Beven, K., 1998. Dynamic real-time prediction of flood inundation probabilities. Hydrological Sciences Journal 43 (2), 181–196.

Romanowicz, R., Beven, K., 2003. Estimation of flood inundation probabilities as conditioned on event inundation maps. Water Resources Research 39 (3), 1–12.

Schäppi, B., Perona, P., Schneider, P., Burlando, P., 2010. Integrating river cross section measurements with digital terrain models for improved flow modelling applications. Computers and Geosciences 36 (6), 707–716.

Schmitt, F.G., 2007. About Boussinesq's turbulent viscosity hypothesis: historical remarks and a direct evaluation of its validity. Comptes Rendus Mécanique 335 (9–10), 617–627.

Schneider, P., Vogt, T., Schirmer, M., Pasquale, N., Doetsch, J., Linde, N., Cirpka, O.A., 2011. Towards improved instrumentation for assessing river–groundwater interactions in a restored river corridor. Hydrology and Earth System Sciences 15, 2531–2549.

Viparelli, E., Gaeuman, D., Wilcock, P., Parker, G., 2011. A model to predict the evolution of a gravel bed river under an imposed cyclic hydrograph and its application to the Trinity River. Water Resources Research 47, W02533.

Wasantha Lal, A.M., 1995. Calibration of riverbed roughness. Journal of Hydraulic Engineering 121 (9), 664–671.

Wohl, E.E., 1998. Uncertainty on flood estimates associated with roughness coefficient. Journal of Hydraulic Engineering 124 (2), 219–223.

Please cite this article as: Pasquale, N., et al., Hydrodynamic model calibration from pattern recognition of non-orthorectified terrestrial photographs. Computers & Geosciences (2013), http://dx.doi.org/10.1016/j.cageo.2013.06.014